View Article Online
View Journal

Nanoscale

Accepted Manuscript

This article can be cited before page numbers have been issued, to do this please use: A. Kumar, F. Colangelo, F. Avitabile, Z. M. Kakhaki, C. Cirillo and C. Attanasio, *Nanoscale*, 2026, DOI: 10.1039/D5NR05284J.

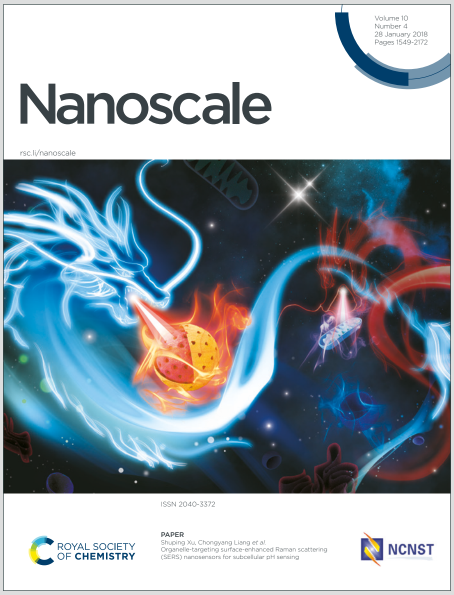

View Article Online
DOI: 10.1039/D5NR05284J

Journal Name

ARTICLE TYPE

Cite this: DOI: 00.0000/xxxxxxxxxx

Received Date
Accepted Date

DOI: 00.0000/xxxxxxxxxx

Fluctuations-Driven Superconductivity in Nitrogen-Doped Disordered Tungsten Rhenium Films

Abhishek Kumar,[*,a,b] F. Colangelo,[a,b] F. Avitabile,[a] Z. Makhdoumi Kakhaki,[†,a,b] C. Cirillo,[a,b] C. Attanasio[a,b,c]

We report a systematic study of nitrogen-doped superconducting tungsten-rhenium (WReN) thin films with thicknesses ranging from 5 to 60 nm, focusing on the interplay of disorder, superconducting fluctuations (SF), quantum fluctuations (QF), and weak localization (WL). The introduction of nitrogen allows fine-tuning of disorder, making WReN an ideal platform to explore quantum transport phenomena compared to related compounds such as WRe. To characterize both superconducting and normal-state properties, we employ Hall effect, magnetoresistance, and magnetoconductivity (MC) measurements for WReN films. Hall measurements provide complementary insight into carrier density, mobility, and disorder in the normal state, while SF, WL, and QF analyses reveal fundamental superconducting parameters, including critical temperature, upper critical field, coherence length and superconducting-insulating transition. Further, MC analyses were used for extracting relaxation times, which were found to be of the order of picoseconds. These results highlight the key role of disorder in shaping both the quantum transport and superconducting behavior of WReN films, offering a foundation for future studies in quantum materials and superconducting device applications.

Introduction

In disordered superconductors, phenomena such as superconducting fluctuations (SF)[1–4], quantum fluctuations (QF)[5–8], and weak localization (WL)[9,10] remain central topics due to their key role in understanding fundamental superconducting properties and their impact on technological applications. These effects govern important phenomena such as quantum phase transitions (QPT)[5–8], vortex dynamics[11–13], and phase slips (PS)[14–16]. A notable example is the quantum Griffiths singularity (QGS)[5–8], a disorder-driven QPT emerging from rare superconducting islands, often associated with superconductor-insulator/metal transition (SIT/SMT), and previously observed in β-tungsten (W) films[7].

Within the W-family superconductors[11–17], materials such as sputtered β-W and FIB-fabricated W have been extensively studied for SIT/SMT, vortex phenomena, phase slips, and fluctuation effects. Incorporating SF and QF analyses enables a detailed exploration of these phenomena across different geometries, including thin films, meanders, and three-dimensional nanohelices. Other W-based compounds, such as tungsten silicide (WSi)[18,19], tungsten germanide (WGe)[20], and FIB-deposited W[21] have demonstrated exceptional performance in superconducting single-photon detectors (SSPDs) and optoelectronic applications[22]. These materials exhibit superconducting critical temperatures (T_c) of 3–6 K, significantly higher than pure W ($T_c \sim 11$ mK[23]), making them suitable for cryogenic operations.

To characterize such superconducting films, temperature-dependent Hall effect measurements provide access to normal-state parameters including carrier density (n_e), Fermi wave vector (k_F, and mean free path (l_e). Together with incorporation of SF[1–3] and WL[9,10], magnetoconductivity analyses under $k_F l_e > 1$ criterion form a comprehensive toolkit for extracting total phase breaking rate (τ_ϕ) and electron energy relaxation times (τ_s), including electron–electron (τ_{e-e}), electron–phonon (τ_{e-ph}), and fluctuation-related (τ_{e-fl}) contributions[4,24–28]. These quantities significantly influence the performances of superconducting devices. For instance, in the case of SSPD, short τ_s enables fast response and low jitter[29,30], while a higher τ_{e-ph}/τ_{e-e} ratio enhances hotspot size and detection efficiency[4,31]. Quasiparticle relaxation processes are further probed via flux-flow instabilities (FFI)[32–35]. Superconductors such as WSi[4,24,28], NbTiN[25], NbN[26], NbGe[27], MoSi[28], WGe[28], NbRe[33], and NbReN[34,35] have been extensively investigated in this context. Based on this, we investigated tungsten rhenium (WRe), a W-family superconductor whose properties can be systematically tuned via nitrogen incorporation[36]. A prior study[37] showed that the WRe and nitrogen-doped WRe (WReN) films deposited on silicon substrates pos-

---

[a] Dipartimento di Fisica "E.R. Caianiello", Università degli Studi di Salerno, I-84084 Fisciano (Sa), Italy. Email: abkumar@unisa.it, abhishekmourya94@gmail.com
[b] CNR-SPIN, c/o Università degli Studi di Salerno, I-84084 Fisciano (Sa), Italy
[c] Centro NANO_MATES, Università degli Studi di Salerno, I-84084 Fisciano (SA), Italy
†Present address: Technische Universität Braunschweig, 38106 Braunschweig, Germany

View Article Online
DOI: 10.1039/D5NR05284J

sess τ_s of the order of picoseconds, comparable to the typical SSPD materials. Furthermore, a 25-nm-thick WReN film, exhibited higher resistivity (ρ) and larger τ_{e-ph}/τ_{e-e} ratios compared to WRe film of the same thickness, indicating improved potential as SSPD material.

In the present study, we examine amorphous WReN films down to the ultrathin limit (5–60 nm) deposited on SiO_2/Si via DC magnetron sputtering. We analyze their superconducting parameters, disorder- and magnetic field- driven QPT, and magnetoconductivity based on SFs and WL. For thinner films (5, 10, 25 nm), we have investigated τ_s and τ_{e-ph}/τ_{e-e} ration incorporating SF and WL contributions, providing insights into their suitability for SSPDs. Temperature-dependent Hall effect measurements complement this analysis by offering information on n_e,k_F, and l_e values. Overall, this work provides new insights into the fundamental properties of WReN and their potential applications in quantum devices and SSPDs.

Experimental Methods

The WReN films were sputtered by a DC magnetron sputtering system on SiO_2/Si substrates using a target of $W_{0.75}Re_{0.25}$ stoichiometry (diameter 5 cm and thickness 3 mm) with a purity of 99.99 % from Testbourne Ltd. The deposition processes were performed at room temperature under an ultra-high vacuum pressure of the order of 2×10^{-8} mbar. By precise control over argon (Ar) and nitrogen (N_2) flow, thus on the $Ar+N_2$ mixture, samples with a concentration of 7.5 % N_2 (of total incoming flux) were prepared by using an optimal fixed sputtering power of 150 W. A calibrated quartz crystal microbalance monitored the sample thickness rate 0.84 Å/s, which was further confirmed using a stylus thickness profilometer (Bruker DektakXT). WReN films with thicknesses 5, 10, 25, 40 and 60 nm were deposited. For simplicity and consistency, these samples are referred to as WN5, WN10, WN25, WN40 and WN60, respectively. A comparative analysis was also performed with WReN and WRe films deposited on Si substrates with a thickness of 25 nm[37]. They are referred to as WN25/Si and W25/Si, respectively.

The X-ray diffraction (XRD) measurements reveal amorphous characteristics for WReN films, consistent with previous studies.[36,37] The scanning electron microscope images (SEM) and energy-dispersive X-ray spectroscopy (EDS) measurements were performed using a ZEISS Sigma 360 instrument equipped with an Oxford Xplore 30 EDS detector. Figure 1(a) shows a SEM image for a WReN film highlighting a uniform surface morphology without evidence of phase segregation, together with the selected EDS mapping area (inset). We note the presence of a surface impurity cluster in the SEM image, which has been intentionally used as a reference feature for focusing purposes. The EDS spectrum shown in Fig. 1(b) displays the characteristic peaks of the detected elements, while the table in the inset reports the compositional analysis in terms of weight percentages obtained from different regions of the sample. Figures 1(c)-(e) show the representative EDS spectra acquired from the mapped region, confirming the presence of well-homogeneous distribution of W, Re, and N across the film.

Superconductivity was studied by performing low-temperature electrical transport measurements in a cryogen-free system (2 K, 7 T) from Cryogenic Ltd. A wire bonder (TPT-wire bonder) was used to obtain four-probe electrical connections in the Van der Pauw configuration. The sheet resistance was measured in a longitudinal direction of current to voltage, while Hall resistance measurements were made in a vertical direction of current to voltage with an excitation current of 10 μA in both cases using a current source Keithley 6121 operating together with a nanovoltmeter Keithley 2182.

Hall Measurements

Figure 2(a) shows the Hall resistivity (ρ_{xy}) measured as a function of the magnetic field (B) in range 0–4 T for the film WN25 at various temperatures (20–300 K), all above T_c. The Hall coefficient, R_H, is extracted from the linear slope of ρ_{xy} versus B, and the corresponding n_e is obtained via $n_e = |-1/(R_H e)|$. The temperature dependence of R_H and n_e for WN25 is plotted in Fig. 2(b) using a dual y-axis scale.

The same analysis was performed for all other samples (WN5, WN10, WN40, and WN60). The corresponding dependence of n_e as a function of temperature is shown in Fig. 2(c). From the n_e values, we further estimated key electronic parameters for all WReN films, including $k_F = (3\pi^2 n_e)^{1/3}$, $l_e = \hbar k_F/(n_e e^2 R_{sn} d)$, and the Fermi velocity $v_F = \hbar k_F/m$. Additionally, the Ioffe–Regel parameter $k_F l_e$ was calculated and its temperature dependence is presented in Fig. 2(d). Interestingly, all these parameters (k_F, n_e, l_e, and $k_F l_e$) are approximately constant throughout the temperature range 20 to 300 K. Temperature-independent n_e confirms the metallic nature of the films, while constant l_e and the fact that $k_F l_e > 1$ indicate that the WReN films are disordered, with transport dominated by defects and impurities[38]. The estimated Hall parameters at 20 K, along with other superconducting parameters, are summarized in Table 1, and compared with those of WN25/Si and W25/Si films.

Superconducting Properties

Figure 3(a) shows the temperature-dependent sheet resistance, $R_s(T)$, for WReN films measured without an external magnetic field in the ranges 3–20 K (main panel) and 3-300 K (inset). We measured normal state resistance (R_{sn}) at 20 K, which increases as the film thickness is reduced, due to the limitation in the electron pathways on decreasing film thicknesses. This behavior can be attributed to Anderson localization, which arises due to enhanced disorder in thinner films. This leads to increased electron scattering, and is associated with SFs and WL effects[1,3]. The BCS mean-field transition temperature (T_c) can be estimated by incorporating the effects of Cooper-pair fluctuations into the resistive transition. These fluctuations are commonly described using the Aslamazov–Larkin (AL)[1,2] and Maki–Thompson (MT)[3,39] models, which are applicable to two-dimensional (2D) or quasi-2D superconductors, and are expressed as:

$$\frac{1}{R_s(T)} = \frac{1}{R_{sn}(T)} + \frac{Ae^2}{16\hbar}\left(\frac{T_c}{T-T_c}\right) \quad (1)$$

Here, $\hbar$ is the Planck constant, e is the elementary charge, and

View Article Online
DOI: 10.1039/D5NR05284J

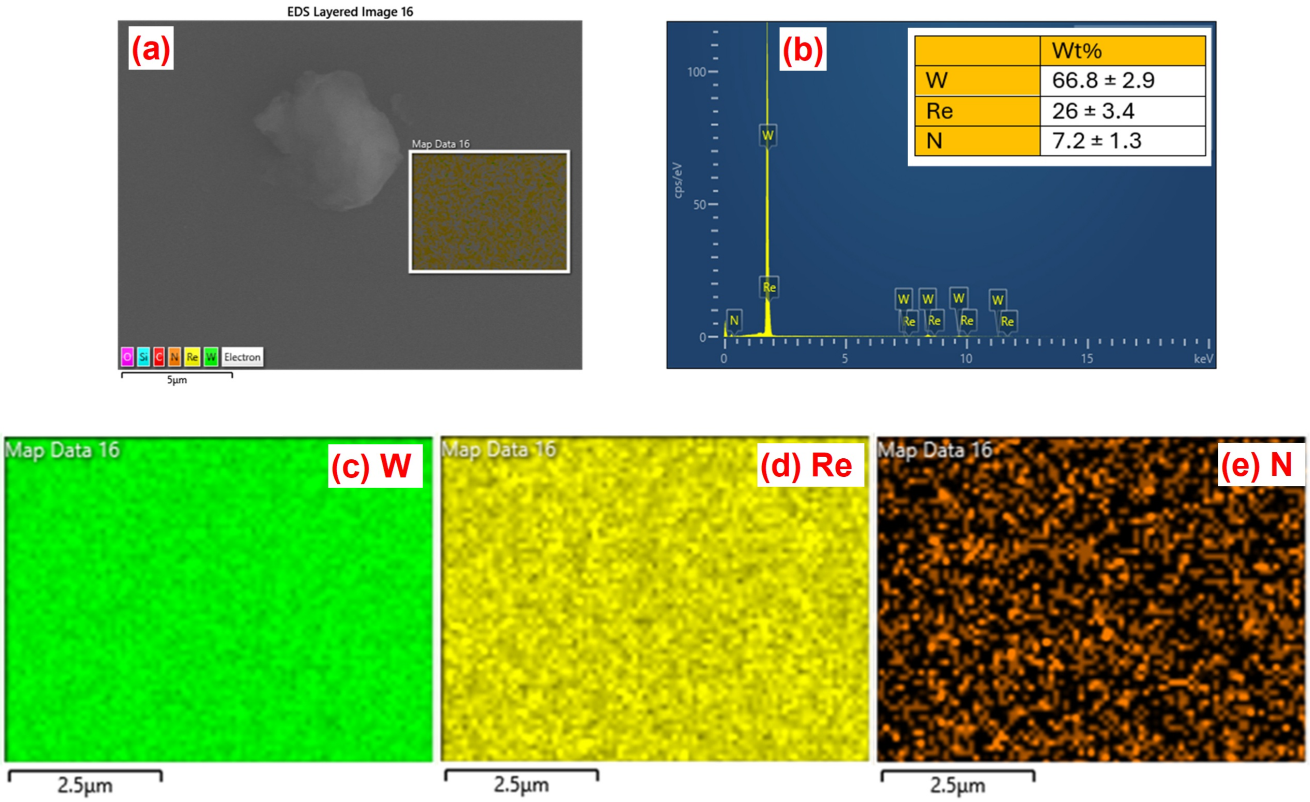

	Wt%
W	66.8 ± 2.9
Re	26 ± 3.4
N	7.2 ± 1.3

Fig. 1 (a) Scanning electron microscopy (SEM) image for a WReN film (60 nm). (b) EDS spectrum with the characteristic elemental peaks of W, Re, and N (main panel), and corresponding weight percentages table (inset). EDS mapping revels a homogeneous distribution of elements- W (c), Re (d), N (e) across the analyzed area.

Table 1 Superconducting transition temperature (T_c), superconducting gap (Δ), normal state resistivity (ρ_n), magnetic penetration depth $[\lambda(0)]$ at 0 K, diffusion constant (D), density of state $N(0)$, charge carrier density (n_e), Fermi wave vector (k_F), mean free path (l_e), Fermi velocity (v_F), for WReN films. These values are also compared with WN25/Si and W25/Si films.[37] d is the thickness of the samples.

Films/ Parameters	d (nm)	T_c (K)	Δ (meV)	ρ_n $(\mu\Omega \cdot cm)$	$\lambda(0)$ (nm)	$D*10^{-4}$ (m^2/s)	$N(0)*10^{47}$ $(m^{-3}J^{-1})$	n_e*10^{29} (e/m^3)	k_F (nm^{-1})	l_e (nm)	v_F*10^6 (m/s)	$Ref.$
WN5	5	4.09	0.61	207	747	0.50	3.75	1.14	15	0.26	1.80	PW*
WN10	10	5.41	0.81	158	568	0.54	4.55	1.39	16	0.3	1.92	PW*
WN25	25	5.79	0.86	158	550	0.56	4.43	1.07	14.7	0.35	1.76	PW*
WN25/Si	25	5.61	0.84	171	581	0.51	4.47	1.19	15	0.31	1.82	[37]
W25/Si	25	4.78	0.71	127	541	0.77	3.99	4.10	23	0.18	2.76	[37]
WN40	40	5.77	0.86	180	587	0.56	3.88	1.11	14.9	0.31	1.79	PW*
WN60	60	5.84	0.87	171	569	0.45	5.02	0.86	13.7	0.38	1.64	PW*

*Present Work

View Article Online
DOI: 10.1039/D5NR05284J

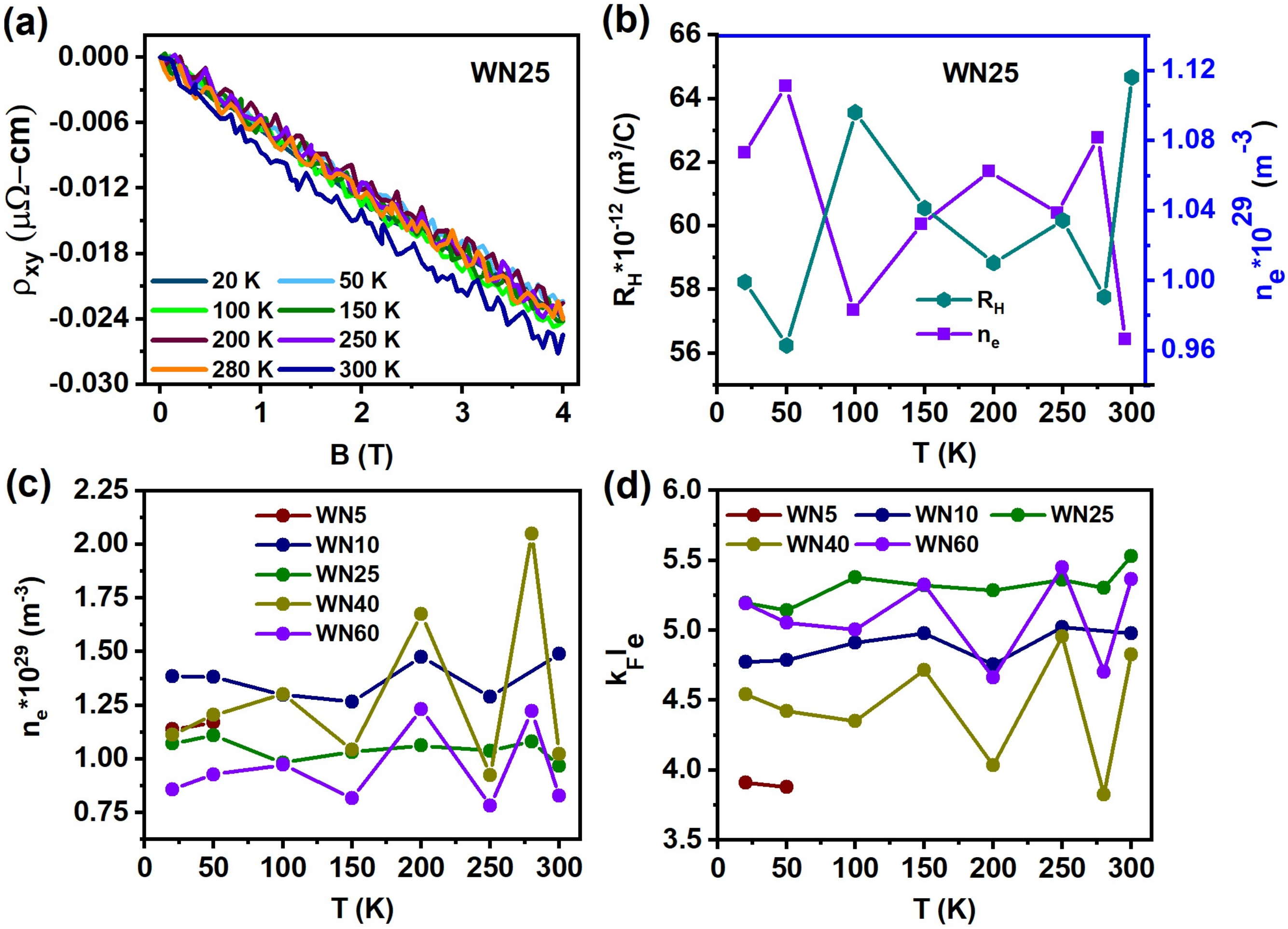

Fig. 2 (a) Magnetic field (B) dependence of the Hall resistivity for the film WN25 at different temperatures. (b) Temperature dependence of the Hall resistance, R_H, (left scale) and charge carrier density, n_e, (right scale) for the sample WN25 sample. (c) Temperature dependence of n_e for all the WReN films. (d) Ioffe-Regel parameter $(k_F l_e)$ as a function of the temperature for all the WReN films.

View Article Online
DOI: 10.1039/D5NR05284J

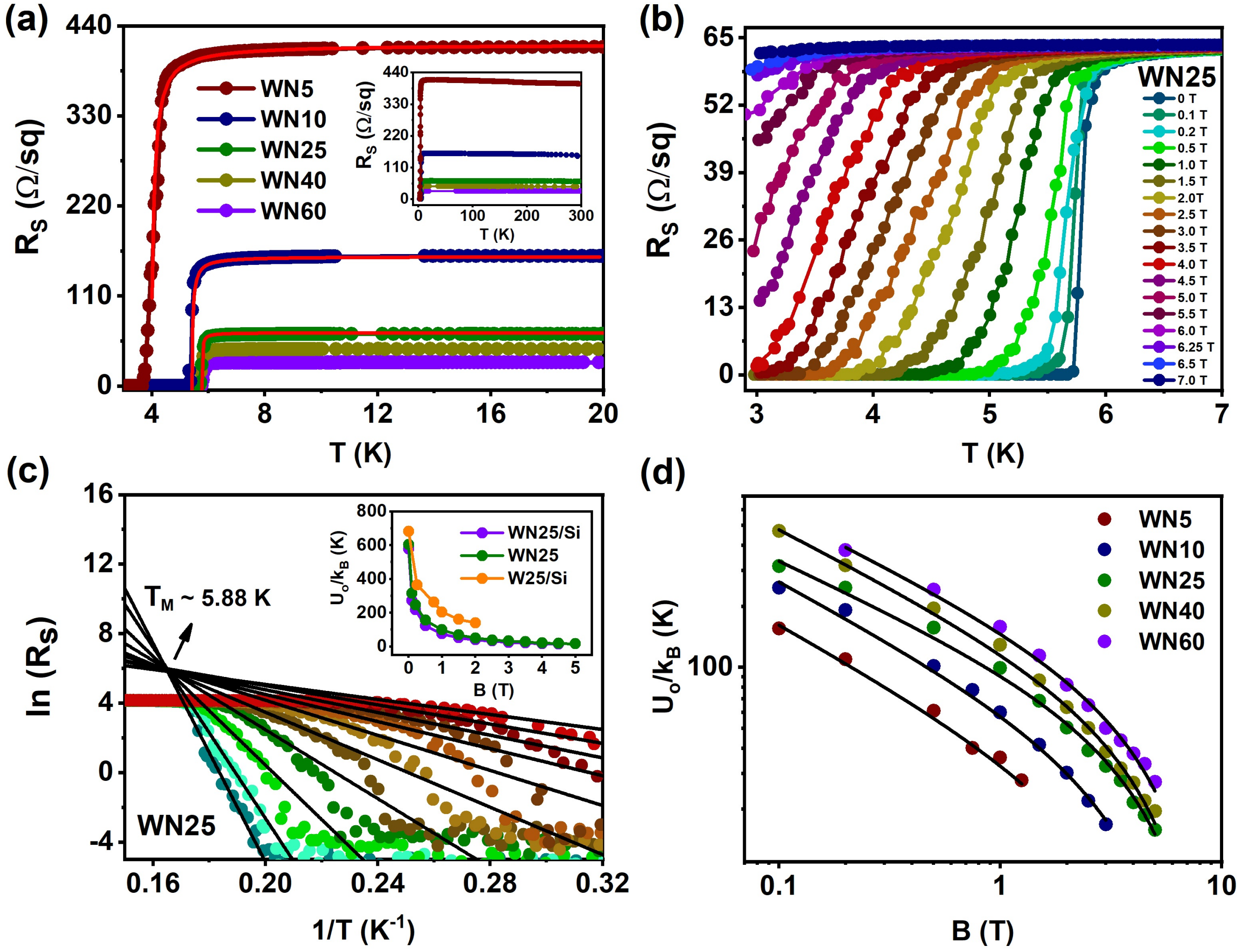

Fig. 3 (a) Superconducting transition curves for WReN films in the temperature range 3-20 K (main panel) and 3-300 K (inset). The red line over experimental data show the fitting of Eq. 1 based on AL and MT fluctuations. (b) R_s-T transition curves measured at different fixed applied magnetic fields (0-7 T) for the WN25 film. (c) The main panel shows the Arrhenius plots of the data of panel (b). The black lines correspond to Arrhenius equation (AE) of thermally activated flux-flow (TAFF) theory. The inset shows the comparison of activation energies as a function of magnetic field for WReN and WRe films 25-nm thick nm (see main text for details). (d) Activation energies as a function of magnetic field for WReN films. The black curves represent the activation energy fit to the experimental data (see main text for details).

View Article Online
DOI: 10.1039/D5NR05284J

we used A and T_c as fitting parameters. The $R_s(T)$ curves are well fitted by following Eq. (1), as shown in Fig. 3(a) by the red curves. We find a good agreement between the T_c values extracted within the $R_{sn}/2$ criteria and those obtained from the fitting procedures (listed in Table 1). The fitted values are $A \sim 3$ for all films. For the thicker films (WN40, WN60), we did not attempt to fit the data using the 2D formula because their higher dimensionality makes such an analysis inappropriate. For WN25, T_c is slightly higher than for WN25/Si. From the inset data of Fig. 3(a), the residual resistance ratio $RRR = R_{sn}^{300K}/R_{sn}^{20K}$ is below unity for all samples, indicating a nearly non-metallic character. In addition, normal-state resistivities (ρ_n) at 20 K are also listed in Table 1. Notably, ρ_n for WN25 lies between the values reported for WN25/Si and W25/Si[36,37]. These ρ_n values were further used to estimate the zero-temperature penetration depth, $\lambda(0) = 1.05 \times 10^{-3}\sqrt{\rho_n/T_c}$[15,40], and the values are listed in Table 1 for all WReN films.

The resistive transitions, $R_s(T)$, in the presence of applied perpendicular B up to 7 T is shown for WN25 in Fig. 3(b), with its Arrhenius-type representation, $\ln R_s$ vs $1/T$, in the main panel of Fig. 3(c). Increasing B shifts superconducting transitions to lower temperatures and broadens them, indicative of thermally activated vortex dynamics.[41–43]. Fitting $R_s(T,B)$ to the Arrhenius relation $R_s(T,B) = R_o(B)\exp(-U_o(B)/k_BT)$ yields activation energies $U_o(B)$, and the fitted black lines crossed at a single-meeting point, $T_M \sim 5.88$ K, close to T_c of WN25. The extracted $U_o(B)$ values are slightly higher than for WN25/Si but lower than for W25/Si[37] (inset of Fig. 3(c)), reflecting the combined effects of substrate and nitrogen doping, which increase disorder and distort vortex structure[44], thereby lowering $U_o(B)$. Here, the obtained activation energies are compatible with values reported for superconducting thin films such as Nb[44] and NbN[45]. Further, Fig. 3(d) summarizes the $U_o(B)$ behavior for all films. The dependence follows $U_o(B) = B^{-a}(1-B/B^*)^b$[46–48], with fitted exponents $a \sim 0.5$ and $b \sim 1.5$, comparable to other superconducting films. The decrease in U_o for thicknesses is attributed to smaller vortex volumes in thinner samples, consistent with FeTeSe films reported elsewhere[49].

The field-dependent superconducting transitions $R_s(B)$ at fixed temperatures are shown in Fig. 4(a–d) for WN5, WN10, WN25, and WN40 films. In all cases, the $R_s(B)$ isotherms exhibit superconducting transition towards lower magnetic fields with increasing temperatures. The temperature dependence of the upper critical fields, $B_{c2}(T)$, extracted using the $R_{sn}/2$ criterion, is plotted in the insets of Fig. 4.

The zero-temperature upper critical field, $B_{c2}(0)$, was obtained by the Werthamer–Hohenberg–Helfand (WHH) theory[50,51]

$$\ln\left(\frac{1}{t}\right) = \sum_{\nu=-\infty}^{\infty}\left[\frac{1}{|2\nu+1|} - \left(|2\nu+1| + \frac{h}{t} + \frac{(\alpha h/t)^2}{|2\nu+1| + (h+\lambda_{so})/t}\right)^{-1}\right], \tag{2}$$

where $t = T/T_c$ and $h = \frac{4}{\pi^2}\frac{B_{c2}(T)}{T_c}\left(\left|\frac{dB_{c2}}{dT}\right|_{T_c}\right)^{-1}$ are the reduced temperature and magnetic field, respectively. α is the Maki parameter and λ_{so} denotes the spin-orbit scattering parameter. The best fittings to the experimental data using Eq. 2 were obtained for $\alpha = 0$ and $\lambda_{\text{so}} = 0$ for all the samples, in agreement with previous analyses on sputtered Nitrogen-doped W thin films[52,53]. The fitted curves are displayed by red color in the insets of Fig.s 4(a)-(d) along with the values of $B_{c2}(0)$ and the zero-temperature coherence lengths, $\xi(0)$ as obtained from $\xi(0) = \sqrt{\phi_0/2\pi B_{c2}(0)}$, with $\phi_0 = h/2e$ the magnetic flux quantum.

The electron diffusion constant was determined from $D = (4k_B/\pi e)(dB_{c2}/dT)^{-1}$, and the density of states from the Einstein relation $N(0) = 1/(De^2R_{sn}d)$, where e is the electronic charge and d the film thickness. The extracted D and $N(0)$ are reported in Table 1. Further, the electron–phonon coupling constant λ_{ep} was estimated from the McMillan formula[54]:

$$\lambda_{ep} = \frac{1.04 + \mu^*\ln(\Theta_D/1.45T_c)}{(1-0.62\mu^*)\ln(\Theta_D/1.45T_c) - 1.04}$$

using $\Theta_D \sim 400$ K for tungsten–rhenium alloys[55] and $\mu^* = 0.1$–0.17[41,56]. For all films, $\lambda_{ep} \sim 0.6$, similar to tungsten carbide[56] and consistent with weak-coupling BCS superconductivity.

We also determined the Pippard coherence length from $\xi_p = \frac{\hbar v_F}{\pi\Delta}$, where $\Delta = 1.76k_BT_c$ is the superconducting gap. The extracted ξ_p values (of the order of hundreds of nanometers for all the films) are much larger than $\xi(0)$, and satisfy the relation

$$\xi(0) \sim (\xi_p l_e)^{1/2} \ll \xi_p,$$

with v_F and l_e taken from the Hall measurements section. This confirms that WReN films are dirty-limit, type-II superconductors, where disorder strongly contributes to their superconducting behavior. Such systems are well known to display fluctuation-driven phenomena at low temperatures[5–8,12–15,43], as discussed in the following sections.

Quantum phase transition (QPT)

Disordered superconductors have long been the subject of intense investigation due to the emergence of QPTs[5–8] governed by QFs. Such transitions can arise from intrinsic disorder, rare-region effects, applied magnetic fields, and temperature-dependent influences on electronic transport. These phenomena are commonly characterized by superconductor-insulator or superconductor-metal transitions (SIT/SMT), exhibiting activated scaling of the resistance with magnetic field and temperature, $R(B,T)$[5,14]. Experimental signatures of these effects have been reported in a variety of superconducting systems, including β-W[7], NbN[57], Ta_2PdS_5[8], MoS_2[6], $MgTi_2O_4$[58], and FIB-deposited W[14].

In our magnetoresistance measurements, we observed that the R_s-$B(T)$ isotherms cross at a single point at higher temperatures (5.5 K to 6.25 K) near T_c for the WN40 sample, as shown in Fig. 5(a). Similar crossing behavior can also be observed at lower temperatures (down to the millikelvin range) and over a broad range of temperatures and magnetic fields for all WReN films, which may be indicative of QGS phenomena[7,8]. We denote the crossing point coordinates as ($R_X = 45.08\ \Omega, B_X = 6.85$ T) in Fig. 5(a). For these disordered WReN films, the QPT is predominantly induced by the applied magnetic field and can be analyzed using finite-size scaling (FSS)[7,8,14]. According to FSS theory[7,8,14], the

View Article Online
DOI: 10.1039/D5NR05284J

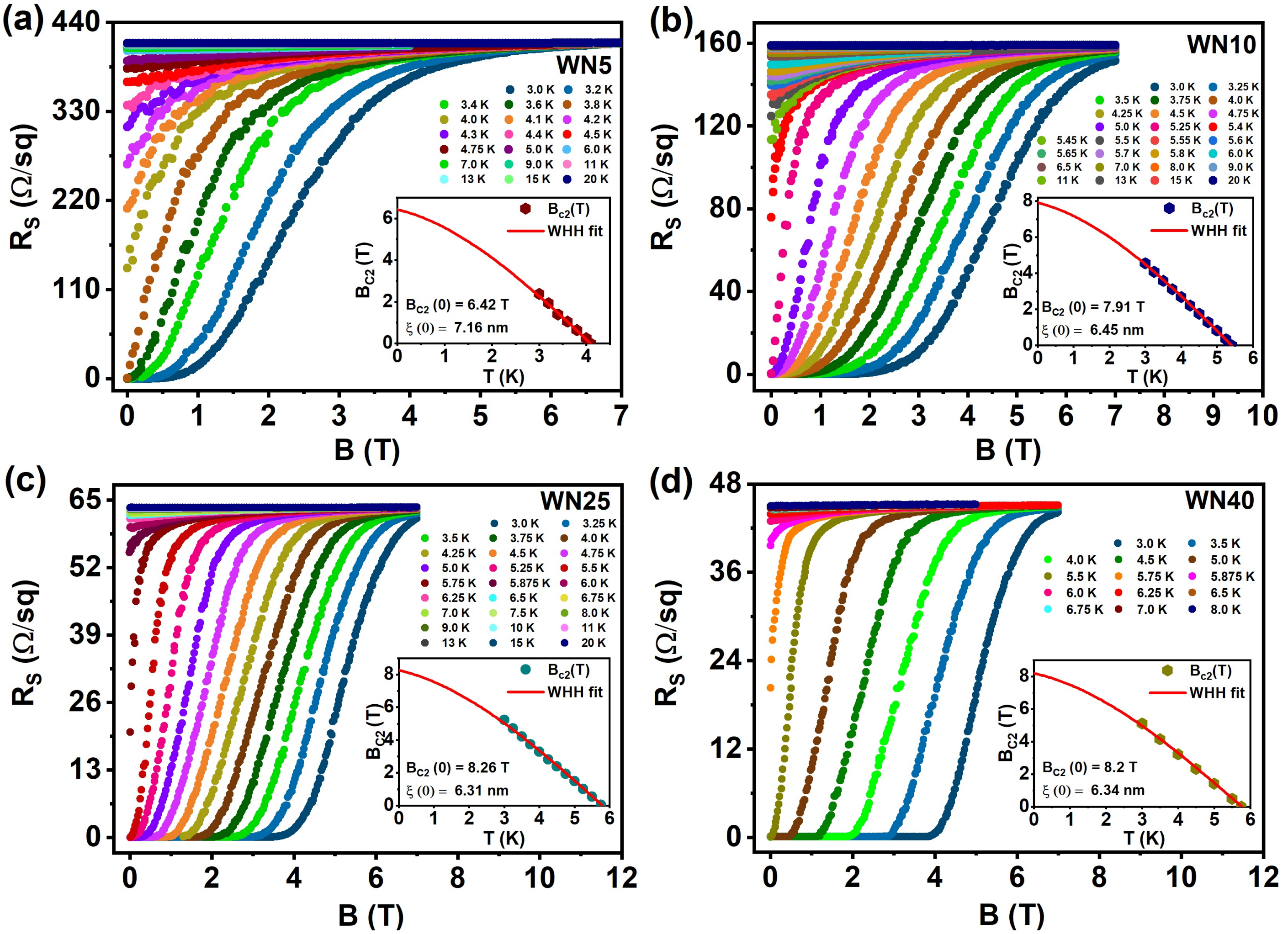

Fig. 4 Sheet resistance (R_s) as a function of the magnetic field at fixed temperatures for samples WN5 (a), WN10 (b), WN25 (c), and WN40 (d). The inset of each panel shows the temperature-dependent upper critical magnetic field, $B_{c2}(T)$, along with the fitting to the experimental data using WHH Eq. (2) as shown by solid red curves.

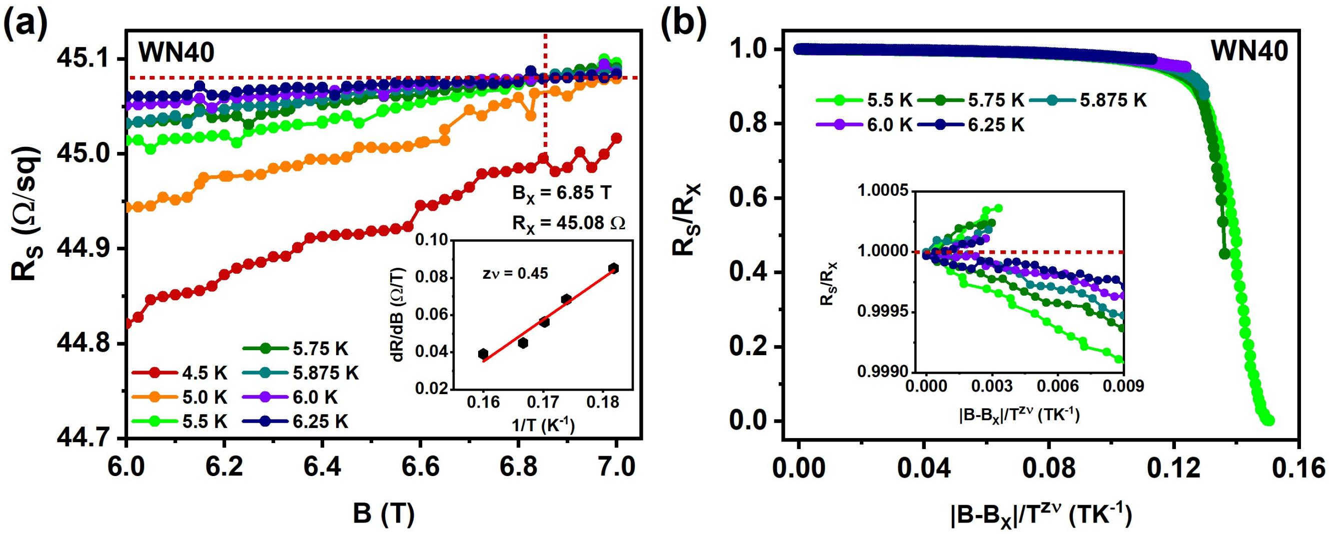

Fig. 5 (a) Sheet resistance (R_s) as a function of the magnetic field for the sample WN40 (main panel) for the high temperature (4.5 - 6.25 K) and high magnetic field (6.0 - 7.0 T) range to show the singular crossing point. The inset shows the corresponding dR/dB versus T^{-1} behavior. Its linear behavior is shown by the red solid line. (b) FFS scaling of the QPT in WN40 film obtained by Eq. (3) for selected temperatures. Inset: zooming of the data in the low field region shows two different behaviors of the $R_s(B,T)$ curves (see main text for details).

View Article Online
DOI: 10.1039/D5NR05284J

resistance near the transition can be expressed as:

$$R(B,T) = R_X\, f\left(\frac{B-B_X}{T^{1/(z\nu)}}\right), \tag{3}$$

where $f(x)$ is a scaling function with $f(0)=1$, and z and ν are the dynamical and correlation-length critical exponents, respectively. The correlation length ξ_c diverges near the QPT as $\xi_c \propto \delta^{-\nu}$ with $\delta = |B-B_X|$, and the characteristic frequency follows $\omega \propto \xi_c^{-z}$ under the influence of QFs. These critical exponents are independent of microscopic details and can be evaluated by plotting dR/dB versus T^{-1} (inset of Fig. 5(a)), where the inverse slope yields the product $z\nu \sim 0.45$ for our WN40 sample. Using Eq. (3), we collapse the $R(B,T)$ curves as shown in Fig. 5(b). The inset clearly demonstrates two distinct behaviors of the scaled resistance above and below unity. The obtained value of $z\nu \sim 0.45$, slightly below 0.66, is consistent with the three-dimensional (3D) nature of the 40 nm WN sample[58]. We note that our measurements are limited by the maximum achievable magnetic field, which constrains a full exploration of the transition. Extending this study to higher fields remains a promising avenue for future work.

Magnetoconductivity and relaxation times

It is well established that magnetoconductivity correction (MC) models[4,24–28] play a crucial role in determining τ_s, which are essential parameters for evaluating the suitability of superconductors in SSPDs. According to the MC model, the total change in magnetoconductivity ($\delta G^{\mathrm{TOTAL}}$) arises from quantum corrections due to several mechanisms: WL, AL, MT, SFs, and density of states (DOS) fluctuations, under the criterion of $k_F l_e > 1$. At temperatures $T \gg T_c$, the dominant contribution to magnetoconductivity originates from WL, a quantum interference effect that occurs in disordered systems. In the presence of a magnetic field, this interference is modified, particularly by spin-orbit scattering, which influences the phase coherence between different electron trajectories. The WL contribution[9,25] to $\delta G^{\mathrm{TOTAL}}$ is given by

$$\delta G^{\mathrm{WL}}(B,T) = \frac{3}{2} Y\left(\frac{B}{\frac{4}{3}B_{\mathrm{so}} + B_\phi}\right) - \frac{1}{2} Y\left(\frac{B}{B_\phi}\right), \tag{4}$$

where $Y(x) = \ln(x) + \psi\left(\frac{1}{2} + \frac{1}{x}\right)$ and ψ is the digamma function. The characteristic magnetic fields $B_{\mathrm{so}} = \hbar/(4eD\tau_{\mathrm{so}})$ and $B_\phi = \hbar/(4eD\tau_\phi)$ correspond to spin–orbit and dephasing scattering, respectively, with τ_{so} denoting the spin–orbit scattering time. As B increases, the magnitude of $\delta G^{\mathrm{WL}}(B,T)$ increases, contributing positively to $\delta G^{\mathrm{TOTAL}}$.

For temperatures $T \sim T_c$, SFs, become prominent due to the formation of short-lived Cooper pairs, resulting in the broadening of the superconducting transition. These fluctuations reduce the effective electron density and enhance the MC. The AL correction[1,2] to $\delta G^{\mathrm{TOTAL}}$ can be expressed as

$$\begin{aligned}\delta G^{\mathrm{AL}}(B,T) = &\frac{\pi^2}{2\ln\left(\frac{T}{T_c}\right)}\left[\frac{B_c}{B}\left\{1 - 2\frac{B_c}{B}.\psi\left(1+\frac{B_c}{B}\right)\right.\right.\\ &\left.\left. + 2\frac{B_c}{B}.\psi\left(\frac{1}{2}+\frac{B_c}{B}\right)\right\} - \frac{1}{4}\right],\end{aligned} \tag{5}$$

where $B_c = Ck_BT/[\pi eD\ln(T/T_c)]$ is the characteristic field, and C is a numerical factor typically ranging between 2 and 6.

Near T_c, the MT correction becomes significant as SFs and electron pairing effects intensify[3,39]. These fluctuations enhance the mean free path l_e and reduce localization effects, thereby increasing the overall MC. The MT correction[3,39,59], formulated by Lopes dos Santos and Abrahams (LSA)[60], is expressed as

$$\delta G^{\mathrm{MT}}(B,T) = -\beta_{\mathrm{LSA}}(T)\left[Y\left(\frac{B}{B_\phi}\right) - Y\left(\frac{B}{B_c}\right)\right], \tag{6}$$

where $\beta_{\mathrm{LSA}}(T) = 2\pi k_B T\hbar^{-1}\left(1/\tau_{\mathrm{GL}} - 1/\tau_\phi\right)^{-1}$, and $\tau_{\mathrm{GL}} = \pi\hbar/[8k_BT\ln(T/T_c)]$ is the Ginzburg–Landau relaxation time. The MT term reflects the interplay between SFs and phase coherence effects.

The final contribution, $\delta G^{\mathrm{DOS}}(B,T)$, arises from fluctuations in the electronic DOS near T_c[61,62]. These variations stem from the energy dependence of the DOS near the Fermi level, which is modified by SFs. The corresponding correction[61] is given by

$$\delta G^{\mathrm{DOS}}(B,T) = \frac{28\zeta(3)}{\pi^2} Y\left(\frac{B}{B_c}\right), \tag{7}$$

where $\zeta(3) = 1.202$. Hence, $\delta G^{\mathrm{TOTAL}}(B,T)$ can be expressed as the summation of all individual correction terms:

$$\begin{aligned}\delta G^{\mathrm{TOTAL}}(B,T) =& \delta G^{\mathrm{WL}}(B,T) + \delta G^{\mathrm{AL}}(B,T)\\ &+ \delta G^{\mathrm{MT}}(B,T) + \delta G^{\mathrm{DOS}}(B,T).\end{aligned} \tag{8}$$

Further, we used the following equation to calculate δG from the experimental data:

$$\delta G(B,T) = \frac{2\pi^2\hbar}{e^2}[R_S^{-1}(B,T) - R_S^{-1}(0,T)], \tag{9}$$

where $R_S^{-1}(B,T)$ and $R_S^{-1}(0,T)$ are the inverse resistances at finite and zero field. Here, we adopted thinner WReN films (WN5, WN10 and WN25) under the criteria of $k_F l_e > 1$ for their relaxation times analysis. Note that the values of $k_F l_e$ were determined from the Hall measurement section. Following Eq. 9, the experimental data (multiple color curved) are shown in Fig. 6(a-c) for all the three samples. Whereas, the well- simulated curves of black color, by following Eq. 8, are shown in 6(a-c) for WN5, WN10 and WN25 samples. From the fits, we extract the total phase scattering rateτ_ϕ values of 7.75 ps (WN5), 26.25 ps (WN10), and 52.91 ps (WN25), which are shorter than those WRe films of comparable thickness[37]. Furthermore, the temperature dependence of τ_ϕ and τ_ϕ^{-1} is shown in Fig. 6(d–f) for all WReN films.

View Article Online
DOI: 10.1039/D5NR05284J

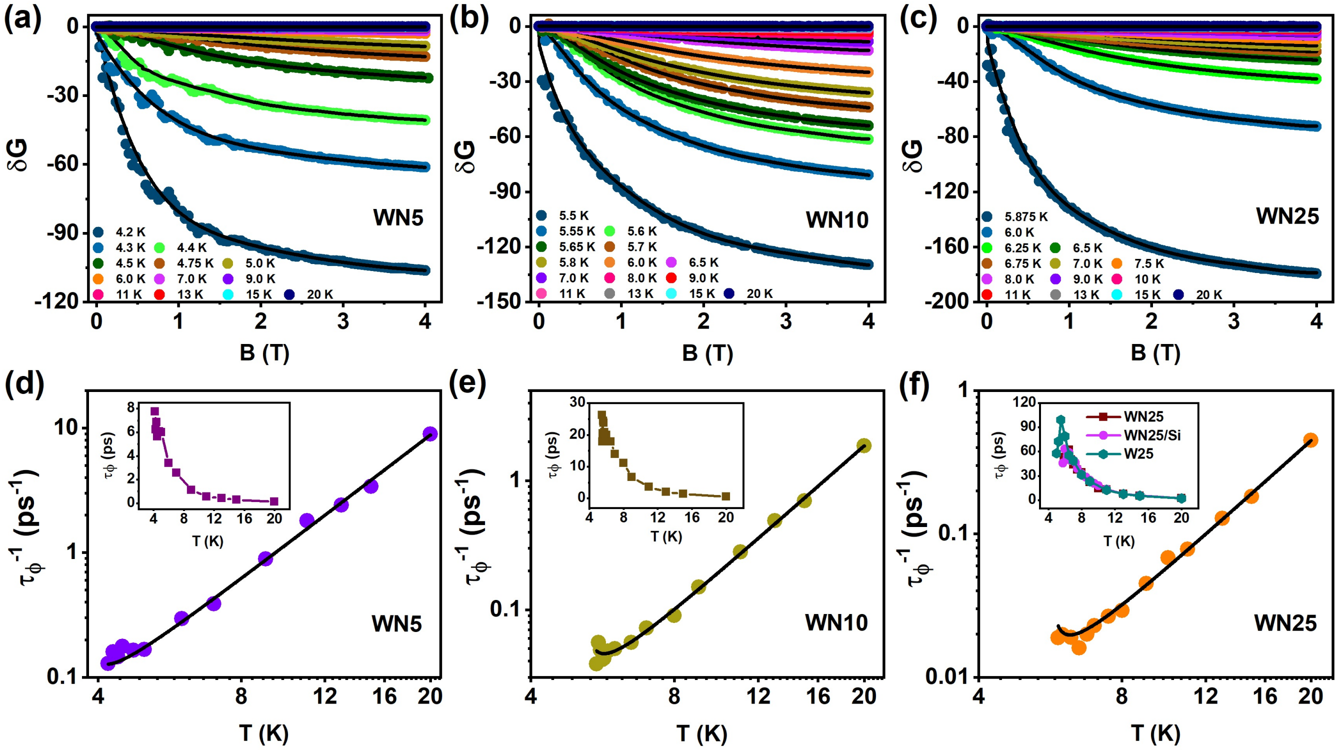

Fig. 6 Total change in magnetoconductivity (δG) as obtained from Eq.(9) at different temperatures for WN5 (a), WN10 (b) and WN25 (c) films. The black lines are the best fit to the data obtained using Eq. (8), which includes corrections in $\delta G(B,T)$ arising from weak localization (WL), Aslamazov-Larkin (AL) fluctuations, Maki-Thompson (MT) fluctuations, and density of states (DOS) fluctuations. Total phase scattering relaxation rate (τ_ϕ) (insets) and its inverse $[\tau_\phi^{-1}(T)]$ (main panel) as a function of the temperature for the films WN5 (d), WN10 (e), and WN25 (f). The black curves are the best fit to the data using Eq. (10). The inset of panel (f) shows the comparison of $\tau_\phi(T)$ for the films WN25, WN25/Si,[37] and W25/Si.[37]

Table 2 Fitting parameters (α_{e-ph} and n) and relaxation times [τ_ϕ, $(\tau_{e-ph})$and (τ_{e-e})] at $T \approx$ 4-6 K as evaluated from Eq.s (10)-(13) for the films in the present study, compared with results from the literature. d is the thickness of the films.

Films	$d(nm)$	$\alpha_{e-ph}\times 10^{-10}$	n	$\tau_\phi(ps)$	$\tau_{e-ph}(ps)$	$\tau_{e-e}(ps)$	τ_{e-ph}/τ_{e-e}	$Ref.$
WN5	5	1.06	2.91	7.75	34.84	23.07	1.51	PW*
WN10	10	0.7	3.25	26.25	49.41	47.06	1.03	PW*
WN25	25	0.99	2.98	52.91	89.48	97.26	0.92	PW*
WN25/Si	25	2.38	2.97	45.70	84.01	91.31	0.92	37
W25/Si	25	1.98	2.95	57.80	94.53	116.7	0.81	37
WSi	5	...	...	9	66	47	1.4	24
WSi	5	55	3.00	6.6	92	24.4	3.8	4
NbTiN	6	31	3.5	52	16.9	...	...	25
NbN	5	10.8	3.53	4.51	9.3	10.8	0.86	26
WGe	5	...	...	...	82	32	2.6	28
MoGe	5	...	...	..	32	28	1.2	28
MoSi	5	...	...	6.67	30	30	1	28

View Article Online
DOI: 10.1039/D5NR05284J

The τ_ϕ can be expressed as

$$\tau_\phi^{-1} = \tau_{e-e}^{-1} + \tau_{e-ph}^{-1} + \tau_{e-fl}^{-1}, \tag{10}$$

where τ_{e-e}, τ_{e-ph}, and τ_{e-fl} are given by following Eq.s (11)–(13).

$$\tau_{e\text{-e}}^{-1} = \frac{k_B T R_{SN} e^2}{2\pi\hbar^2} \ln\left(\frac{\pi\hbar}{e^2 R_{SN}}\right), \tag{11}$$

$$\tau_{e\text{-ph}}^{-1} = \alpha_{e\text{-ph}}^{-1} \left(\frac{T}{T_c}\right)^n, \tag{12}$$

$$\tau_{e\text{-fl}}^{-1} = \frac{k_B T R_{SN} e^2}{2\pi\hbar^2} \cdot \frac{2\ln 2}{\ln\left(\frac{T}{T_c}\right) + \gamma}, \tag{13}$$

where $\gamma = \frac{4\ln 2}{\sqrt{\ln^2\left(\frac{\pi\hbar}{e^2 R_{SN}}\right) + \frac{128\hbar}{e^2 R_{SN}}} - \ln\left(\frac{\pi\hbar}{e^2 R_{SN}}\right)}$, and $\alpha_{e\text{-ph}}$ and n are fitting parameters. The well-simulated curves over experimental $\tau_\phi(T)$ data using Eq. (10) are shown by black color in Fig. 6(d–f) for all WReN films and the fit parameters summarized in Table 2. Furthermore, we also extracted $\tau_{e-ph}(T)$ and plotted in Fig. 7 together with fits (black lines) using Eq. (12) for WN5, WN10 and WN25 films.

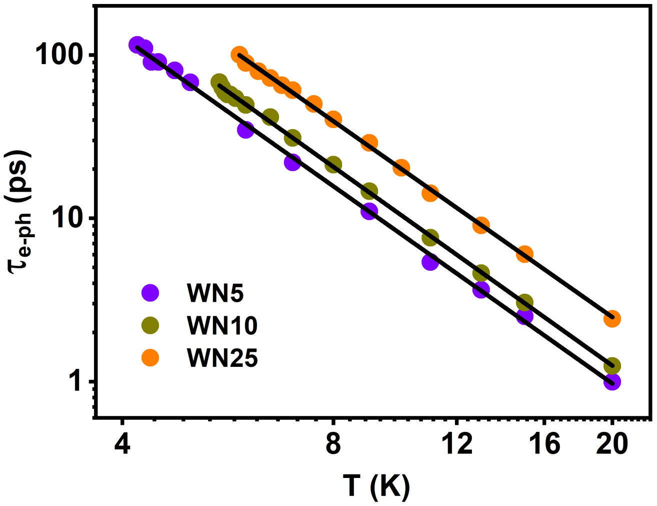

Fig. 7 τ_{e-ph} as a function of the temperature for the samples WN5, WN10 and WN25 films. The black lines show the best fit to the data by following Eq. (12).

Discussion

We investigated the effect of disorder on the superconducting and normal-state properties of amorphous WReN thin films by combining Hall transport, fluctuation conductivity, magnetoresistance, and quantum scaling analyses. The results establish a consistent picture in which nitrogen incorporation increases disorder, thereby reshaping both the electronic landscape and the superconducting ground state.

Hall measurements demonstrate that nitrogen systematically reduces carrier mobility and enhances scattering, confirming the emergence of a disorder-dominated normal state. This is consistent with the reduced residual-resistivity ratios ($RRR < 1$) and with the non-metallic temperature dependence associated with localization effects. The superconducting transition reflects these modifications: SF analyses (AL, and MT terms) show that a higher nitrogen content correlates with enhanced T_c, larger $B_{c2}(0)$, and correspondingly shorter coherence lengths $\xi(0)$. These trends highlight the role of controlled disorder in strengthening superconducting pairing in amorphous WReN, in contrast to crystalline alloys where disorder is typically detrimental.

Magnetic field–dependent $R(T)$ curves reveal thermally activated flux-flow behavior, with activation energies $U(B)$ that decrease at high magnetic fields. This indicates weakened pinning and enhanced vortex mobility, consistent with increased thermal activation of the vortices in highly disordered films. A slight substrate dependence larger $U(B)$ for films grown on SiO_2/Si suggests that interface disorder and strain modulate vortex dynamics and can serve as an additional tuning parameter for flux motion.

A clear crossing point in the magnetoresistance isotherms indicates a magnetic field–driven QPT and may lead to the existence of QGS phenomena. The extracted critical exponent $z\nu \approx 0.45$ lies within the range characteristic of 3D QPTs. Although this value does not conclusively demonstrate a QGS, the trends are compatible with enhanced QFs in the presence of strong disorder, the full range of $z\nu$ need further investigation to clarify. Further measurements in a broad range of temperatures and higher magnetic fields are needed to establish whether WReN hosts a Griffiths-like regime.

Magnetoconductivity analysis provides additional insight into quasiparticle relaxation relevant for nonequilibrium superconducting dynamics. The disorder enhances electron–electron scattering while modifying electron–phonon coupling, reflected in the short dephasing times τ_ϕ and in the increased ratios $\tau_{e\text{-}ph}/\tau_{e\text{-}e}$ obtained for the WReN films than pure WRe[37], particularly for WN5 ($\tau_\phi - 7.75 ps$ and $\tau_{e\text{-}ph}/\tau_{e\text{-}e} - 1.51$). These values fall within the range reported for well-established SSPD materials, such as WSi, NbN, NbTiN, WGe, and MoSi, as mentioned in Table 2. Although our study focuses on fundamental transport mechanisms rather than device performance, the extracted relaxation parameters indicate that WReN shares key microscopic features with materials employed in SSPDs.

We can now discus the suitability of WReN thin films for the realization of SSPDs. The first observation is that nitrogen incorporation during deposition leads to disorderness and amorphous characteristics for WReN films. This represents an advantage for uniformity, reduced constrictions and defects, and higher fabrication tolerance, also in terms of substrate choice. Further, short order of relaxation times with the larger $\tau_{\mathrm{e-ph}}/\tau_{\mathrm{e-e}}$ ratio, suggests an efficient energy transfer from the photon to the electronic system, with a positive impact on efficiency. This finding is promising also for the realization of micrometric detectors (SMSPDs)[63]. Interestingly, the $\tau_{\mathrm{e-ph}}/\tau_{\mathrm{e-e}}$ ratio is compatible with those of other tungsten-based materials, such as WSi and WGe[28]. On the contrary, the characteristic $\tau_{\mathrm{e-e}}$ time scales are shorter than those of amorphous materials, and this can potentially result in devices with improved time performance, in particular in shorter dead times. Regarding the superconducting properties, the values of T_c are very similar to those of amorphous superconductors perform-

View Article Online
DOI: 10.1039/D5NR05284J

ing as good SNSPDs (WSi, WGe, MoSi) and lower than crystalline NbN, NbTiN. In particular, T_c of WReN is intermediate between Re-based superconductors used in this field, namely NbRe[64,65] and NbReN[66]. This tunable, relatively low-T_c can be suitable for the detection of low-energy infrared photons used in quantum communication, LIDAR, and satellite communications. Finally, the short coherence length also supports ultrathin-film device fabrication while preserving superconducting properties, making it a promising material for efficient SSPDs. The practical implementation of the WReN films in SSPDs in meander form is currently the subject of active research and ongoing investigation.[67]

Overall, our results demonstrate that WReN thin films represent a versatile platform in which disorder can be tuned to manipulate SFs, vortex dynamics, and quantum interference effects. The observation of a field-driven QPT, together with signatures of pronounced QFs, makes WReN a promising system for exploring quantum phase transitions in disordered superconductors. Future work involving broader nitrogen concentrations, lower-temperature scaling, and direct photon-detection experiments will clarify the microscopic mechanisms and further assess the potential of WReN for quantum electronic technologies.

Conclusions

We deposited WReN films of different thicknesses (5–60 nm) on SiO_2 substrates by DC magnetron sputtering, which show amorphous and disordered characteristics. The films exhibit superconducting transition temperatures $T_c \sim$ 4–6 K, upper critical fields $B_{c2}(0) \sim 8$ T, and coherence lengths $\xi(0) \sim 6$ nm.

The thermally activated vortex dynamics is observed, with behavior influenced by the film thickness, substrate, and nitrogen content. In the 40 nm film, a disorder- and field-induced quantum phase transition near T_c highlights the role of QFs. Hall measurements (20–300 K) indicate nearly constant normal-state parameters, confirming metallic transport with moderate disorder. Magnetoconductivity analysis of thinner films (5–25 nm) reveals short phase relaxation times and enhanced τ_{e-ph}/τ_{e-e} ratios than pure WRe, comparable to established SSPD materials (WSi, NbN, NbTiN, WGe, MoSi).

These results establish WReN films as promising candidates for superconducting and quantum devices, particularly single-photon detectors, and provide a foundation for further studies exploring disorder, vortex dynamics, and energy relaxation in these systems.

Conflicts of interest

There are no conflicts to declare.

Acknowledgements

This research was partially supported by the project IR0000003−IRIS, supported by the NextGeneration EU funded Italian National Recovery and Resilience Plan with the Decree of the Ministry of University and Research number 124 (21/06/2022) for Mission 4 − Component 2 − Investment 3.1. This research was also partially supported by the project "High-performance Josephson junctions for ferrotransmons – CONJUNCTIONS" in the frame of Partenariato Esteso "NQSTI", Spoke 5, funded by the Italian National Recovery and Resilience Plan Mission 4, Component 2, Investment 3.1.

References

1 L. G. Aslamazov and A. I. Larkin, in *Effect of fluctuations on the properties of a superconductor above the critical temperature. In: 30 Years of the Landau Institute-Selected Papers*, World Scientific, 1996, pp. 23–28.
2 L. Aslamasov and A. Larkin, *Phys. Lett. A*, 1968, **26**, 238–239.
3 K. Maki, *Prog. Theor. Phys.*, 1968, **40**, 193–200.
4 X. Zhang, A. E. Lita, M. Sidorova, V. B. Verma, Q. Wang, S. W. Nam, A. Semenov and A. Schilling, *Phys. Rev. B*, 2018, **97**, 174502.
5 Z. Wang, Y. Liu, C. Ji and J. Wang, *Rep. Prog. Phys.*, 2024, **87**, 014502.
6 Y. Saito, T. Nojima and Y. Iwasa, *Nat. Commun.*, 2018, **9**, 778.
7 C. Huang, E. Zhang, Y. Zhang, J. Zhang, F. Xiu, H. Liu, X. Xie, L. Ai, Y. Yang, M. Zhao, J. Qi, L. Li, S. Liu, Z. Li, R. Zhan, Y.-Q. Bie, X. Kou, S. Deng and X. Xie, *Sci. Bull.*, 2021, **66**, 1830–1838.
8 E. Zhang, J. Zhi, Y.-C. Zou, Z. Ye, L. Ai, J. Shi, C. Huang, S. Liu, Z. Lin, X. Zheng, N. Kang, H. Xu, W. Wang, L. He, J. Zou, J. Liu, Z. Mao and F. Xiu, *Nat. Commun.*, 2018, **9**, 4656.
9 S. Hikami, A. I. Larkin and Y. Nagaoka, *Prog. Theor. Phys.*, 1980, **63**, 707–710.
10 W. Brenig, *J. Low Temp. Phys.*, 1985, **60**, 297–322.
11 I. Guillamón, H. Suderow, A. Fernández-Pacheco, J. Sesé, R. Córdoba, J. M. De Teresa, M. R. Ibarra and S. Vieira, *Nat. Phys.*, 2009, **5**, 651–655.
12 R. Córdoba, T. I. Baturina, J. Sesé, A. Y. Mironov, J. M. De Teresa, M. R. Ibarra, D. A. Nasimov, A. K. Gutakovskii, A. V. Latyshev, I. Guillamón, H. Suderow, S. Vieira, M. R. Baklanov, J. J. Palacios and V. M. Vinokur, *Nat. Commun.*, 2013, **4**, 1437.
13 Y. Sun, J. Wang, W. Zhao, M. Tian, M. Singh and M. H. W. Chan, *Sci. Rep.*, 2013, **3**, 2307.
14 R. P. Aloysius, S. Husale, A. Kumar, F. Ahmad, A. K. Gangwar, G. S. Papanai and A. Gupta, *Nanotechnology*, 2019, **30**, 405001.
15 A. Kumar, S. Husale, M. P. Saravanan, B. Gajar, M. Yousuf, A. Saini, M. G. Yadav and R. P. Aloysius, *Nanotechnology*, 2023, **35**, 015705.
16 R. Córdoba, D. Mailly, R. O. Rezaev, E. I. Smirnova, O. G. Schmidt, V. M. Fomin, U. Zeitler, I. Guillamón, H. Suderow and J. M. De Teresa, *Nano Lett.*, 2019, **19**, 8597–8604.
17 A. Kumar, S. Husale, H. Pandey, M. G. Yadav, M. Yousuf, G. S. Papanai, A. Gupta and R. P. Aloysius, *Eng. Res. Express.*, 2021, **3**, 025017.
18 H. L. Jeannic, V. B. Verma, A. Cavaillès, F. Marsili, M. D. Shaw, K. Huang, O. Morin, S. W. Nam and J. Laurat, *Opt. Lett.*, 2016, **41**, 5341–5344.
19 F. Marsili, V. B. Verma, J. A. Stern *et al.*, *Nat. Photon.*, 2013, **7**, 210–214.

View Article Online
DOI: 10.1039/D5NR05284J

20 S. Yang, Y. Chen, L. Sun, H. Zhou, Y. Li, J. Huang, X. Zheng, R. Ma, J. Xiong, Z. Wan, X. Liu, H. Li, J. Zheng, W. Peng, X. Zhang and L. You, *Appl. Phys. Lett.*, 2025, **126**, 162601.

21 C. García-Pérez, F. J. Urbanos, G. Caballero, M. R. Osorio, A. Gómez, R. Bernardo-Gavito and D. Granados, *Materials Today Quantum*, 2025, 100043.

22 A. Kumar, A. Sharma, A. Pandey, M. P. Saravanan and S. Husale, *Mater. Adv.*, 2023, **4**, 4138–4150.

23 J. W. Gibson and R. A. Hein, *Phys. Rev. Lett.*, 1964, **12**, 688–690.

24 X. Zhang, A. Engel, Q. Wang, A. Schilling, A. Semenov, M. Sidorova, H.-W. Hübers, I. Charaev, K. Ilin and M. Siegel, *Phys. Rev. B*, 2016, **94**, 174509.

25 M. Sidorova, A. D. Semenov, H.-W. Hübers, S. Gyger, S. Steinhauer, X. Zhang and A. Schilling, *Phys. Rev. B*, 2021, **104**, 184514.

26 M. Sidorova, A. Semenov, H.-W. Hübers, K. Ilin, M. Siegel, I. Charaev, M. Moshkova, N. Kaurova, G. N. Goltsman, X. Zhang and A. Schilling, *Phys. Rev. B*, 2020, **102**, 054501.

27 M. G. Yadav, M. Yousuf, M. M. Sharma, P. Pratap, A. Kumar, A. Saini, V. P. S. Awana, V. G. Achanta and R. P. Aloysius, *Supercond. Sci. Technol.*, 2024, **37**, 115025.

28 P. Ercolano, X. Zhang, G. P. Pepe and L. You, *Supercond. Sci. Technol.*, 2025, **38**, 015011.

29 A. Engel, J. J. Renema, K. Il'in and A. Semenov, *Supercond. Sci. Technol.*, 2015, **28**, 114003.

30 D. Vodolazov, N. Manova, Y. Korneeva and A. Korneev, *Phys. Rev. Appl.*, 2020, **14**, 044041.

31 C. M. Natarajan, M. G. Tanner and R. H. Hadfield, *Supercond. Sci. Technol.*, 2012, **25**, 063001.

32 A. I. Larkin and Y. N. Ovchinnikov, *Sov. Phys. JETP*, 1975, **41**, 960.

33 M. Caputo, C. Cirillo and C. Attanasio, *Appl. Phys. Lett.*, 2017, **111**, 192601.

34 C. Cirillo, V. Granata, A. Spuri, A. Di Bernardo and C. Attanasio, *Phys. Rev. Mater.*, 2021, **5**, 085004.

35 Z. Makhdoumi Kakhaki, A. Leo, A. Spuri, M. Ejrnaes, L. Parlato, G. Pepe, F. Avitabile, A. Di Bernardo, A. Nigro, C. Attanasio and C. Cirillo, *Mater. Sci. Eng. B*, 2024, **304**, 117376.

36 F. Colangelo, F. Avitabile, Z. Makhdoumi Kakhaki, A. Kumar, A. Di Bernardo, C. Bernini, A. Martinelli, A. Nigro, C. Cirillo and C. Attanasio, *Phys. Rev. Mater.*, 2025, **9**, 114802.

37 A. Kumar, F. Colangelo, F. Avitabile, Z. Makhdoumi Kakhaki, C. Cirillo and C. Attanasio, *Supercond. Sci. Technol.*, 2026, **39**, 025017.

38 V. Palenskis and V. Jonkus, *Metals*, 2023, **13**, 1551.

39 R. S. Thompson, *Phys. Rev. B*, 1970, **1**, 327–333.

40 L. P. Gor'kov, *Sov. Phys. JETP*, 1959, **36**, 1918–1923.

41 M. Tinkham, *Introduction to Superconductivity*, McGraw-Hill, New York, 2nd edn., 2004.

42 M. Feigel'man, V. Geshkenbein and A. Larkin, *Phys. C Supercond.*, 1990, **167**, 177–187.

43 A. W. Tsen, B. Hunt, Y. D. Kim, Z. J. Yuan, S. Jia, R. J. Cava, J. Hone, P. Kim, C. R. Dean and A. N. Pasupathy, *Nat. Phys.*, 2016, **12**, 208–212.

44 S. M. Altanany, I. Zajcewa, T. Zajarniuk, A. Szewczyk and M. Z. Cieplak, *Phys. Rev. B*, 2024, **109**, 214504.

45 T.-Y. Jing, Z.-Y. Han, Z.-H. He, M.-X. Shao, P. Li and Z.-Q. Li, *Phys. Rev. B*, 2023, **107**, 184515.

46 J. R. Thompson, K. D. Sorge, C. Cantoni, H. R. Kerchner, D. K. Christen and M. Paranthaman, *Supercond. Sci. Technol.*, 2005, **18**, 970–976.

47 S. Pandya, S. Sherif, L. S. S. Chandra and V. Ganesan, *Supercond. Sci. Technol.*, 2011, **24**, 045011.

48 J. Hänisch, K. Iida, F. Kurth, E. Reich, C. Tarantini, J. Jaroszynski, T. Förster, G. Fuchs, R. Hühne, V. Grinenko, L. Schultz and B. Holzapfel, *Sci. Rep.*, 2015, **5**, 17363.

49 F. Tang, P. Wang, P. Wang, Y. Gan, G. D. Gu, W. Zhang, M. He and L. Zhang, *J. Phys.: Condens. Matter.*, 2019, **31**, 265702.

50 N. R. Werthamer, E. Helfand and P. C. Hohenberg, *Phys. Rev.*, 1966, **147**, 295–302.

51 E. Helfand and N. R. Werthamer, *Phys. Rev.*, 1966, **147**, 288–294.

52 J. Hofer and N. Haberkorn, *Thin Solid Films*, 2019, **685**, 117–122.

53 J. A. Hofer, S. Bengio, S. Suárez and N. Haberkorn, *Mater. Adv.*, 2023, **4**, 150–156.

54 W. L. McMillan, *Phys. Rev.*, 1968, **167**, 331–344.

55 S. W. Liu, C. Q. Xu and J. Y. Zhang, *J. Supercond. Nov. Magn.*, 2020, **33**, 1317–1321.

56 H. Chakraborti, B. P. Joshi, C. K. Barman, A. K. Jain, B. Pal, B. C. Barik, T. Maiti, R. Schott, A. D. Wieck, M. J. N. V. Prasad, S. Dhar, H. K. Pal, A. Alam and K. Das Gupta, *Appl. Phys. Lett.*, 2022, **120**, 132601.

57 X. Wang, L. Wang, Y. Liu, F. Chen, W. Gao, Y. Wu, Z. Xu, W. Peng, Z. Wang, Z. Di, W. Li, G. Mu and Z. Lin, *Phys. Rev. B*, 2023, **107**, 094509.

58 S. Qi, Y. Liu, Z. Wang, F. Chen, Q. Li, H. Ji, R. Li, Y. Li, J. Fang, H. Liu, F. Wang, K. Jin, X. C. Xie and J. Wang, *Phys. Rev. Lett.*, 2024, **133**, 226001.

59 A. I. Larkin, *JETP Lett.*, 1980, **31**, 239.

60 J. M. B. Lopes dos Santos and E. Abrahams, *Phys. Rev. B*, 1985, **31**, 172–176.

61 A. Glatz, A. A. Varlamov and V. M. Vinokur, *Europhys. Lett.*, 2011, **94**, 47005.

62 A. I. Larkin and A. A. Varlamov, in *The Physics of Superconductors*, Springer, Berlin, Heidelberg, 2003, pp. 95–231.

63 D. Y. Vodolazov, *Phys. Rev. Appl.*, 2017, **7**, 034014.

64 C. Cirillo, J. Chang, M. Caputo, J. W. N. Los, S. Dorenbos, I. Esmaeil Zadeh and C. Attanasio, *Appl. Phys. Lett.*, 2020, **117**, 172602.

65 M. Ejrnaes, C. Cirillo, D. Salvoni, F. Chianese, C. Bruscino, P. Ercolano, A. Cassinese, C. Attanasio, G. P. Pepe and L. Parlato, *Appl. Phys. Lett.*, 2022, **121**, 262601.

66 F. Avitabile, F. Colangelo, M. Y. Mikhailov, Z. Makhdoumi Kakhaki, A. Kumar, I. Esmaeil Zadeh, C. Attanasio and C. Cirillo, *Appl. Phys. Lett.*, 2025, **127**, 172601.

View Article Online
DOI: 10.1039/D5NR05284J

67 F. Colangelo, A. Kumar, H. Wang, F. Avitabile, C. Attanasio, I. Esmaeil Zadeh and C. Cirillo, *arXiv preprint arXiv:2605.25597*, 2026.

View Article Online
DOI: 10.1039/D5NR05284J

The data that represent the results of this paper and the data that support the findings of this study are available from the corresponding author upon reasonable request.